Crystallographic Characterisation of Hydrogen-induced Twin Boundary Separation in Type 304 Stainless Steel Using Micro-tensile Testing

Ueki, Shohei
Department of Materials Science and Engineering, Kumamoto University

Koga, Kaoru
Department of Materials Science and Engineering, Kumamoto University

Mine, Yoji
Department of Materials Science and Engineering, Kumamoto University

Takashima, Kazuki
Department of Materials Science and Engineering, Kumamoto University

出版情報：ISIJ International. 59 (5), pp.927-934, 2019-05-15. 一般社団法人日本鉄鋼協会
バージョン：

ISIJ International, Vol. 59 (2019), No. 5, pp. 927–934

Crystallographic Characterisation of Hydrogen-induced Twin Boundary Separation in Type 304 Stainless Steel Using Micro-tensile Testing

Shohei UEKI,[1] Kaoru KOGA,[2] Yoji MINE[1]* and Kazuki TAKASHIMA[1]

1) Department of Materials Science and Engineering, Kumamoto University, 2-39-1 Kurokami, Chuo-ku, Kumamoto, 860-8555 Japan.
2) Department of Materials Science and Engineering, Kumamoto University. Now at KYOCERA Industrial Tools Corporation, 762 Mesaki-cho, Fuchu-shi, Hiroshima, 726-0033 Japan.

(*Received on September 5, 2018; accepted on November 27, 2018*)

Micro-tensile behaviour and the corresponding microstructural evolution under hydrogen pre-charging conditions were examined on single-crystalline and twinned bi-crystalline specimens with the same [111] loading axis to elucidate the hydrogen-induced twin boundary separation in type 304 stainless steel. A hydrogen pre-charge increased the flow stress during tensile testing but decreased the elongation-to-failure in both single-crystalline and twinned specimens. Although the hydrogen-charged single-crystalline specimen exhibited a quasi-cleavage, the presence of a twin boundary induced a premature failure at the twin boundary interface. Flat-facetted features due to the twin boundary separation had linear steps in the three $<1\bar{1}0>$ directions, which corresponded to the intersections between the twin plane and the other {111} close-packed planes of austenite. Matching halves of the fracture surface along the three directions perpendicular to the linear steps, *i.e.* $<11\bar{2}>$ on the (111) twin plane, revealed two sets of concavity–flat surface and a peak-and-valley correspondence. In addition, electron backscatter diffraction analysis of the substructures below the fracture surfaces revealed that martensite variants developed mainly with their habit planes parallel to the most favourably shear-stressed plane in each crystal, and they grew towards the concavities on the fracture surfaces. These findings suggest that the hydrogen-induced twin boundary separation is triggered by cracks generated by the high hydrogen concentration at the twin boundary due to deformation-induced martensitic transformation, and this is followed by coalescence of cracks through hydrogen-enhanced alternating shear on the slip planes situated symmetrically with respect to the twin boundary.

KEY WORDS: metastable austenitic steel; hydrogen embrittlement; twin boundary; martensitic transformation; micro-tensile testing.

1. Introduction

The understanding of the underlying mechanism for the hydrogen embrittlement (HE) is an important issue to ensure the safety of a hydrogen-based energy system. Like type 316L stainless steel, stable austenitic steels have been used in the hydrogen industry, because of their low susceptibility to HE. Decreasing the Ni content of austenitic stainless steels not only reduces their costs but also strengthens them. However, susceptibility to HE in the austenitic steels has been reported to depend largely on the stability of the austenitic phase.[1–4] The low stability of austenitic phase increases the occurrence of flat facets and quasi-cleavages in a hydrogen-rich environment,[5–8] which deteriorates the mechanical properties under monotonic[5–10] and cyclic[11–15] loading conditions. Like type 304 stainless steel, metastable austenitic steels containing less Ni content suffer from more severe HE, which is attributed to deformation-induced martensitic transformations.[5–15] Micro-tensile testing using the hydrogen-charged type 304 single crystal revealed[16] that quasi-cleavage occurs along the habit planes of martensite/austenite lamellae that have been formed during the deformation process. Meanwhile, the formation of flat facets is supposed to be due to twin boundary separation.[6–8,17–19] Caskey has reported[6,17] that twin boundary parting is characterised by the following features. A single facet extends over a single grain. Three sets of {111} plane traces appear on the facets and one set of traces is more predominant than the others. Based on the fractographic observation, he supposed that the traces arise from intersection of a facet face with slip, deformation-induced ε– or α'–martensite. However, there has been no direct evidence showing the interplay between twin boundary and deformation-induced martensite. In addition, Jackson *et al.* have proposed[18] the hydrogen-induced crack growth mechanism that does not need the contribution of deformation-induced martensite. It is suggested that hydrogen-induced twin boundary separation

* Corresponding author: E-mail: mine@msre.kumamoto-u.ac.jp
DOI: https://doi.org/10.2355/isijinternational.ISIJINT-2018-608

proceeds by linking of many micro-voids formed at the line of intersection between deformation bands and twin boundaries. Recently, the authors performed a fatigue crack growth test[19] using a small twinned bi-crystalline specimen of a type 304 steel with hydrogen pre-charge and examined the fatigue surface matching by means of electron backscatter diffraction (EBSD) analysis. It was found[19] that the microstructures developed at flat-faceted surface and its counterpart mostly feature a combination of martensite and austenite. In addition, the flat-faceted features more frequently appeared at lower temperatures, where deformation-induced martensitic transformation readily occurred.[18] These statements suggest that deformation-induced martensitic transformation plays a crucial role in the hydrogen-induced twin boundary separation mechanism in metastable austenitic steels.

With regard to martensitic transformation due to a chemical driving force, twenty-four variants of martensite can be formed from a single austenite grain according to the Kurdjumov–Sachs (K–S) orientation relationship expressed as $(111)_A//(011)_M$ and $[\bar{1}\,01]_A//[\bar{1}\,\bar{1}\,1]_M$, where subscripts A and M denote austenite and martensite, respectively. When the martensitic transformation was assisted by a mechanical driving force, it was revealed[20,21] that martensite variants having a habit plane in common were chosen, which were formed by the first shear along $\{111\}_A < \bar{1}\,\bar{1}\,2>_A$ with the most favourably resolved shear stress. In other words, the variant selection of martensite during deformation depends strongly on the relationship between the stress direction and the crystallographic orientation of the parent austenite grain. Therefore, in the present study, the authors performed micro-tensile tests on twinned bi-crystalline specimens of type 304 metastable austenitic steel with hydrogen pre-charge, with focus on the relationship between fracture surface geometry of flat-faceted features and martensite structures developed by deformation.

2. Material and Methods

The material used in this sturdy was a type 304 (JIS-SUS304) austenitic stainless steel, composed of 0.05C, 18.54Cr, 8.09Ni, 0.58Si, 1.24Mn, 0.025P, 0.003S (in mass%), and Fe for the remainder. Coarse-grained samples with a grain size of several tens of micrometres were obtained through heat treatment at a temperature of 1 403 K for 2 h followed by water quenching. These samples were thinned to a thickness of ~30 μm through grinding with emery paper and diamond paste. Both surfaces of the samples were electro-chemically polished for EBSD analysis. The crystal orientation was determined using a scanning electron microscope (SEM) equipped with an EBSD analyser and TexSEM Laboratories software OIM v.7.1.0. Micro-tensile specimens with a gauge section of 20 μm × 20 μm × 50 μm were fabricated using focused ion beam (FIB). Single-crystalline (SC) specimens and twinned bi-crystalline (TW) specimens were prepared with their loading directions (LDs) nearly parallel to [111] direction. For the TW specimens, the twin boundary was set perpendicular to the LD. **Figure 1** shows the shapes of the TW specimens, where the ones with and without subsequent hydrogen charge are distinguished by the suffixes "-H" and "-U", respectively. A small fraction of martensite is visible along the twin boundary at the top face in TW-U and TW-H (circled by dashed lines in Figs. 1(a) and 1(b), respectively), since FIB fabrication readily induces martensite along a twin boundary. By contrast, no martensite was observed along the twin boundary (Fig. 1(c)). A set of specimens were cathodically charged with hydrogen in H_2SO_4 aqueous solution (pH = 3.5) held at 353 K with a current density of 27 A m^{-2}. Based on an estimate of the diffusion velocity,[4] the charging time was chosen in a manner that the 20 μm thick specimen would be saturated with hydrogen. These charging conditions can provide a saturated hydrogen concentration of ~100 mass ppm for a type 304 stainless steel.[16] Tensile tests were started within 3 h after hydrogen charging through cutting the gauge part supporting members using a laser beam. Tensile tests were performed at room temperature under laboratory atmospheric conditions and at a displacement rate of 0.1 μm s^{-1}, corresponding to a strain rate of 2×10^{-3} s^{-1}. The setup is described in more detail elsewhere.[22] The gauge section of the tensile specimen was monitored during tensile testing using an optical microscope (OM) in order to dynamically measure the strain as a function of time. For post-failure EBSD analysis, some samples were further fabricated using FIB to make a longitudinal cut. The crystal orientations were determined using automatic beam scanning with a step size of 0.08 μm at an accelerating

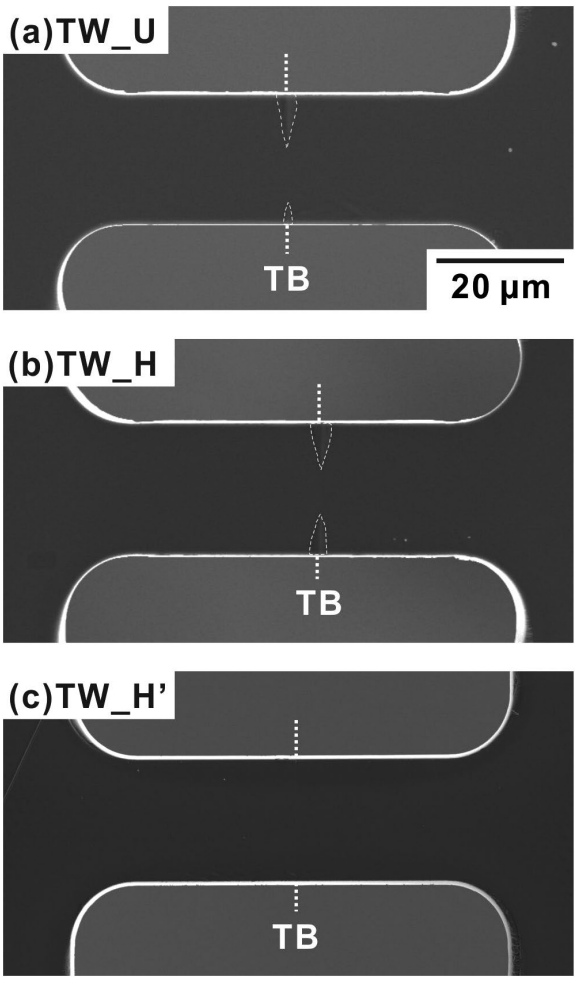

Fig. 1. SEM images of the (a) TW-U, (b) TW-H and (c) TW-H' specimens in the initial state. Region marked by arrows in (a) and (b) show a small fraction of martensite, and TB indicates the twin boundary.

voltage of 20 kV. For the flat fracture surfaces formed in the TW-H' specimen, three-dimensional (3D) area analyses were carried out using Alicona MeX software. A 3D stereographic image was constructed with three SEM micrographs of different tilt angles of ±6° and 0°. In addition, the substructures below the flat fracture surfaces were examined by automatic beam scanning with a step size of 0.008 μm at an accelerating voltage of 30 kV through transmission EBSD (t-EBSD). Samples for t-EBSD were milled perpendicularly to the flat fracture surfaces.

3. Results and Discussion

Figure 2 shows the true stress–true strain, σ_T–ε_T, relationships calculated from the nominal stress–nominal strain, σ_0–ε_0, curves obtained by micro-tensile testing. Here, σ_T and ε_T are calculated using the following equations: $\sigma_T = \sigma_0 (1+\varepsilon_0)$ and $\varepsilon_T = \ln (1+\varepsilon_0)$. Since these equations can be applied for the uniform elongation regime, we focus on the σ_T–ε_T behaviour until the onset of plastic instability. The arrows in the figure indicate the onset of plastic instability, where necking occurs in the tensile specimens. Both hydrogen-charged specimens fractured prior to the onset of plastic instability. Similar to the polycrystalline bulk specimens,[23] the solute hydrogen increases the flow stress, but decreases the elongation-to-failure in both SC and TW specimens. The yield stress in the SC specimens was increased by hydrogen from ~267 to ~448 MPa, which could be attributed to a solute solution strengthening effect, as previously shown in the SC specimens with the [123] loading axis (from ~169 MPa to ~231 MPa).[16] The SC-H specimen exhibits two-step work hardening after the onset of yielding, whereas the SC-U specimen shows nearly linear hardening behaviour. It should be noted that the work hardening rate significantly increases at the stage II of SC-H. Comparison between the uncharged specimens reveals that the work hardening rate right after the onset of yielding is higher in TW-U than in SC-U. This indicates that the twin boundary affects the early stage of work hardening behaviour. In addition, the TW-H specimen exhibits a high work hardening rate, compared to the SC-H specimen and fractures prior to reaching the stage II of the work hardening. This implies that the presence of the twin boundary accelerates the failure process under the hydrogen pre-charging conditions.

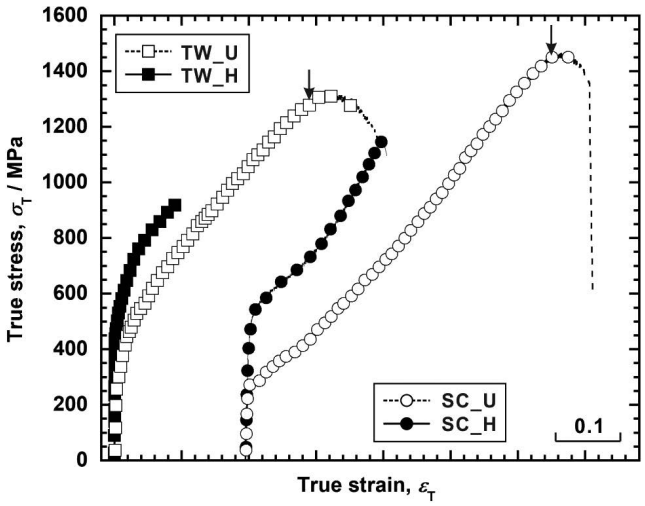

Fig. 2. True stress–strain curves for the (a) SC and (b) TW specimens.

Figure 3 shows the deformation processes of the SC-U and SC-H specimens with the [111] loading axis. In the SC-U specimen, slip steps appeared along two directions corresponding to the first and the second highest shear stressed {111} planes on the top surface of the specimen immediately after the onset of yielding (Fig. 3(a)). Unlike the SC-U specimen with the [123] loading axis,[16] an easy glide stage was not observed in the stress–strain behaviour for the [111] SC-U specimen in the present study (Fig. 2). This is due to the fact that the three $\{111\}_A$ slip planes were almost equally shear-stressed. At the true strain of 0.23 for the SC-U specimen, ill-defined undulation, which is different from slip steps, began to appear (Fig. 3(b)). This undulation can be presumably attributed to martensitic transformation, as previously reported by Tsurui *et al.*[24] With respect to the SC-H specimen, ill-defined undulation

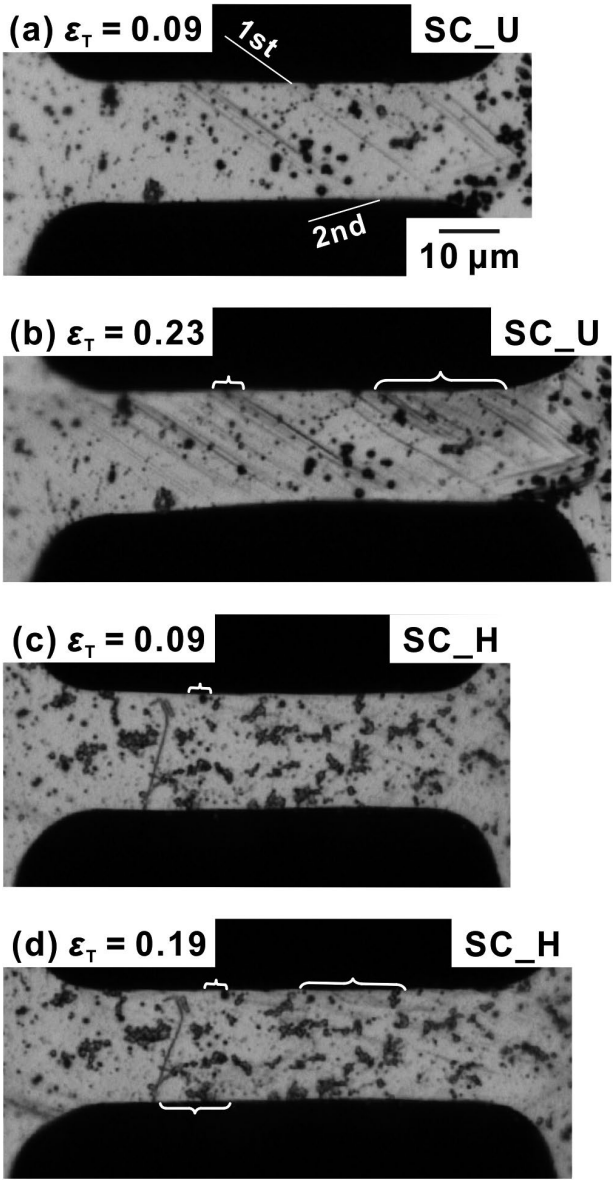

Fig. 3. Optical micrographs showing the deformation processes of the (a and b) SC-U and (c and d) SC-H specimens. The flecks on the specimen surface are debris arising from cutting the supporting members for the gauge section using laser beam.

appeared without development of slip bands immediately after the onset of yielding (Fig. 3(c)). X-ray diffraction measurements by Pontini and Hermida[25] revealed that hydrogen charging into a type 304 stainless steel decreased the stacking fault energy. These suggest that the mechanical driving force required for martensitic transformation was decreased by solute hydrogen, leading to martensitic transformation at an early stage of work hardening (Fig. 2). In fact, martensitic transformation occurred at an early stage of deformation in the SC-H specimen with the loading axis around [110].[16] At the stage II of the [111] SC-H specimen, undulation was spread throughout the gauge section of the specimen, concurrently with the activation of the multiple shear systems (Fig. 3(d)).

Figure 4 shows the fracture morphology and deformation microstructure in the SC-U and SC-H specimens. **Table 1** compares the highest Schmid factors (SFs) for each {111} close packed plane in the parent austenite, assuming the operation of the $\{111\}_A<11\bar{2}>_A$ shear systems. This table helps to predict the martensite variants to be formed in the SC-U and SC-H specimens. Here, the $\{111\}_A$ planes are labelled CP-1 to CP-4, in order of the highest SFs. The insets in Figs. 4(a) and 4(b) show the EBSD colour-coded maps, which distinguish martensite variants of SC-U and SC-H specimens after fracture, respectively. Figures 4(c) and 4(d) show the $(011)_M$ pole figures of martensite corresponding to colour-coded maps in Figs. 4(a) and 4(b), respectively. The EBSD analysis reveals that martensite variants with their habit planes parallel to CP-1, CP-2, and CP-3 were formed in both SC-U and SC-H specimens. There was no difference in the martensite variant selection with regard to distinguishing the habit planes of martensitic transformation.

Figures 5(a) and 5(b) show the fracture surfaces of SC-U and SC-H, respectively, with the [111] loading axis. The fracture surface of the SC-H specimen was characterised by quasi-cleavages with steps corresponding to the habit planes of CP-1, CP-2 and CP-3 martensite variants (Fig. 5(b)), whereas the SC-U specimen exhibited a shear fracture with significant necking (Fig. 5(a)). Similar to [123] SC-H specimen,[16] the hydrogen-induced quasi-cleavage occurred along habit planes of martensite formed during deformation in the [111] SC-H specimen. It is noteworthy that the region where the martensitic transformation takes place is spatially limited, owing to hydrogen-enhanced slip planarity.[26] If hydrogen-containing austenite is transformed to martensite, excess hydrogen is generated therein and diffuses to the neighbouring austenite. This is due to the fact that the diffusivity of hydrogen is high but its solubility is low in martensite, compared to austenite.[27] Considering these arguments, it is plausible that excess-hydrogen-enhanced slip localisation in the retained austenite increased the work

Table 1. Highest Schmid factors of $\{111\}_A<112>_A$ shear systems in each shear plane of the SC-U and SC-H specimens.

Specimen	Symbol	Shear plane	Shear direction	Schmid factor
SC-U	CP-1	$(1\bar{1}1)_A$	$[121]_A$	0.33
	CP-2	$(11\bar{1})_A$	$[112]_A$	0.32
	CP-3	$(\bar{1}11)_A$	$[211]_A$	0.31
	CP-4	$(111)_A$	$[11\bar{2}]_A$	0
SC-H	CP-1	$(1\bar{1}1)_A$	$[121]_A$	0.34
	CP-2	$(1\bar{1}\bar{1})_A$	$[211]_A$	0.31
	CP-3	$(\bar{1}\bar{1}1)_A$	$[112]_A$	0.29
	CP-4	$(111)_A$	$[11\bar{2}]_A$	0

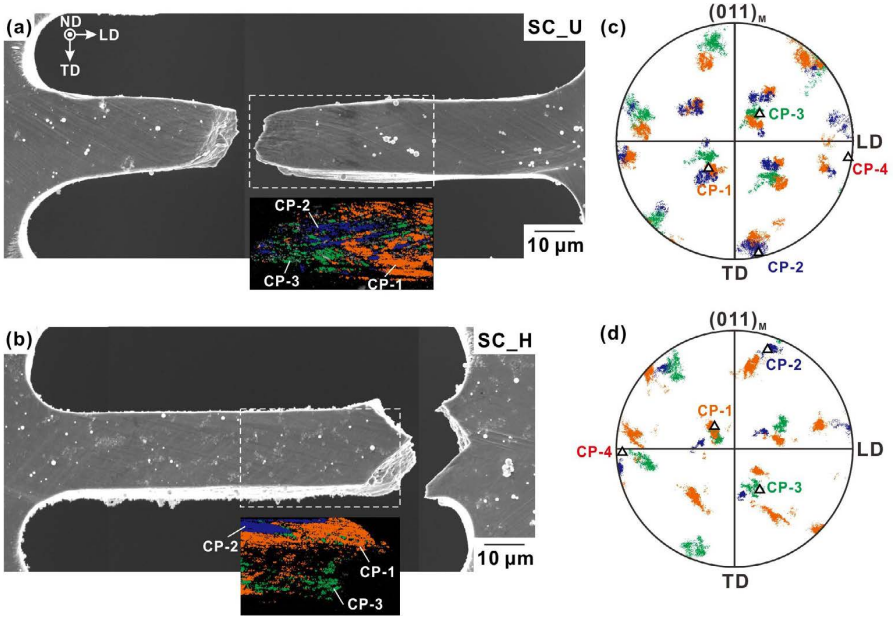

Fig. 4. SEM micrographs comparing the fracture morphology of the (a) SC-U and (b) SC-H specimens. The insets in (a and b) show the EBSD colour-coded maps—which distinguish martensite variants— taken in the areas marked by the boxes. The flecks on the specimen surface are debris arising from cutting the supporting members for the gauge section using laser beam. (c and d) $(011)_M$ pole figures of martensite corresponding to the colour-coded maps in (a and b), respectively (orange, blue, and green marks represent CP-1, CP-2, and CP-3, respectively). The areas in grey and black correspond to points indexed as austenite and non-indexed patterns, respectively. (Online version in color.)

hardening rate of the stage II in the SC-H specimen (Fig. 2), ultimately leading to premature fracture with quasi-cleavages along the CP-1, CP-2, and CP-3 planes (Fig. 5(b)).

Figure 6 shows the deformation process and the fracture morphology in the TW-U specimen. At the initial stage of work hardening in the TW-U specimen, no definite slip bands were developed near the twin boundary (Fig. 6(a)), while deformation spread across the twin boundary at the latter stage (Fig. 6(b)). Finally, the TW-U specimen fractured in the right-hand crystal with significant necking (Fig. 6(c)). Therefore, without hydrogen, twin boundary contributes only to the initial stage of work hardening.

Figure 7 shows the fracture morphology of the TW-H and TW-H' specimens. In both hydrogen-charged TW specimens, the final fracture occurred at the twin boundary interface (Figs. 7(a) and 7(b)), and the fracture surfaces exhibited flat-faceted feature with linear steps in three directions (Figs. 7(c) and 7(d)). Figure 7(e) shows the $(111)_A$ pole figure of the parent austenite along the loading direction of the TW-H specimen. The directions of three sets of linear steps observed on the fracture surface coincide with the intersections between the twin plane and the other {111} slip planes in both austenite crystals (Figs. 7(c) and 7(e)). In the TW-H specimen, necking seemed to occur at the part, where mar-

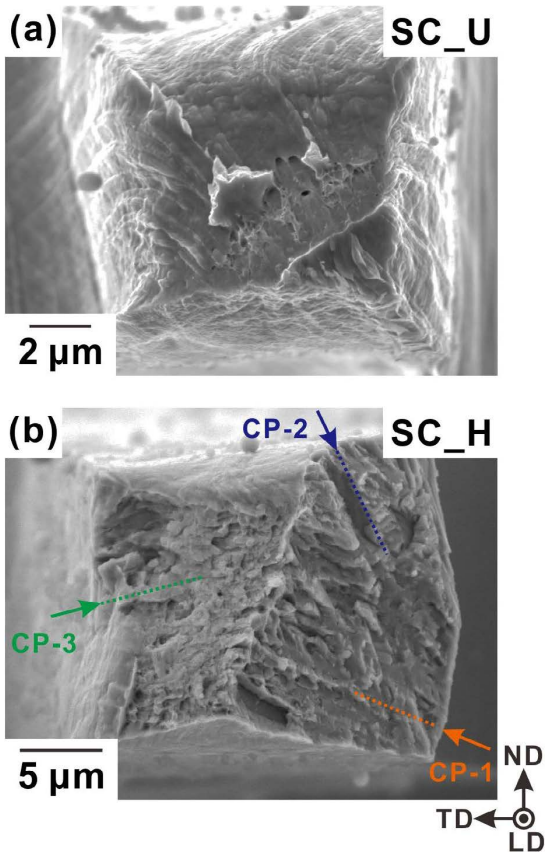

Fig. 5. SEM micrographs comparing the fracture surfaces of the (a) SC-U and (b) SC-H specimens. (Online version in color.)

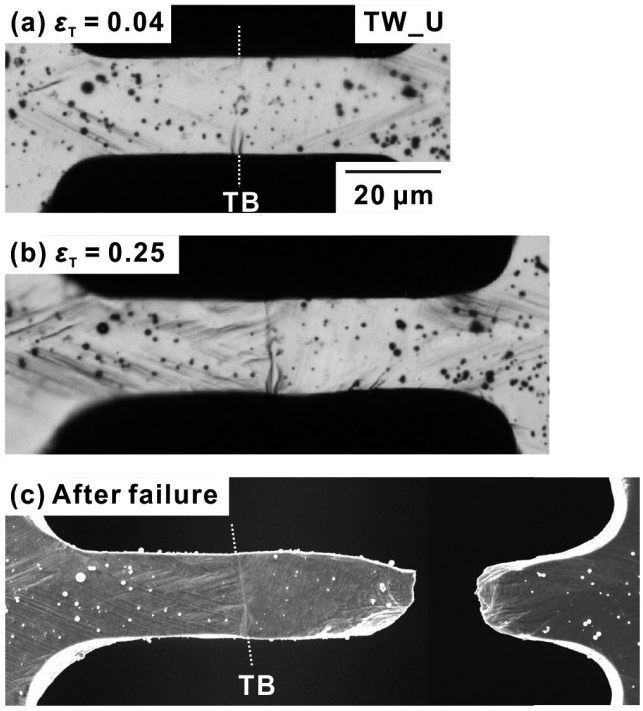

Fig. 6. (a and b) optical micrographs showing the deformation process and (c) SEM micrograph of fracture morphology after failure in the TW-U specimen. The flecks on the specimen surface are debris arising from cutting the supporting members for the gauge section using laser beam.

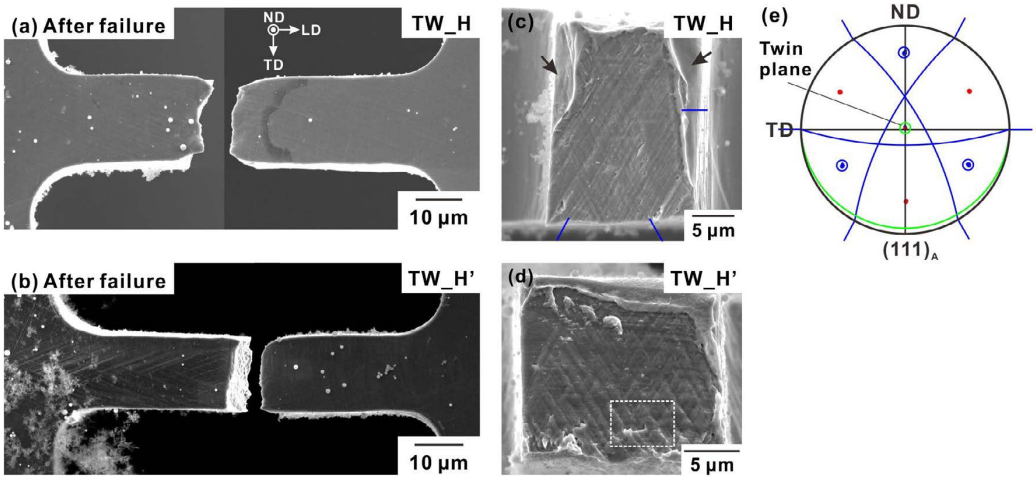

Fig. 7. SEM micrographs showing the fracture morphology of the (a and c) TW-H and (b and d) TW-H' specimens, (e) $(111)_A$ pole figure of parent austenite corresponding to (c), obtained at the top surface using EBSD. The flecks on the specimen surface are debris arising from cutting the supporting members for the gauge section using laser beam. (Online version in color.)

tensite had existed prior to tensile testing (marked by arrows in Fig. 6(c)), and therefore the pre-existing martensite was plastically deformed, even under hydrogen pre-charging conditions. Although there is no pre-existing martensite at the twin boundary in the TW-H' specimen (Fig. 1(c)), similar necking appeared at a final fracture part (Fig. 6(d)). Thus, it makes no significant difference in the fracture morphology, whether martensite existed at the twin boundary prior to tensile loading or not. The TW-H specimens fractured at a lower strain than the SC-H specimen did. This indicates that the hydrogen-induced twin boundary separation preceded hydrogen-induced quasi-cleavage. It was also found[16] that the twin boundary separation does not occur in the case, where the twin boundary is oriented parallel to the loading axis for the TW specimen, and the quasi-cleavage occurs in each crystal along the primary slip systems. Therefore, these are competitive HE mechanisms, which depend on twin boundary orientation with respect to the LD.

Figure 8 presents the correspondence of fracture surface profiles of the TW-H' specimen based on 3D-SEM analysis. Figures 8(a) and 8(b) show the SEM micrographs of flat-faceted feature boxed in Fig. 7(d) and its counterpart, respectively. Figures 8(c) and 8(d) show the $(111)_A$ pole figures along LD in the left- and right-hand crystals (denoted as L and R crystals), respectively. The line profiles in Figs. 8(e), 8(f), and 8(g) were analysed on both halves of the fracture surfaces (Figs. 8(a) and 8(b)), as marked by A–A′, B–B′, and C–C′, respectively. These directions were perpendicular to the linear steps, *i.e.* $<11\bar{2}>$ on the (111) twin plane. The linear steps perpendicular to A–A′ in each crystal correspond to the intersection of the twin plane with the CP-1 plane for the L crystal and the CP-3 plane for the R crystal. In addition, concavities were formed on the fracture surface of the L crystal and correspond to the flat surface on the fracture surface of R crystal (indicated by arrows in Fig. 8(e)). Similar to the correspondence of the A–A′ profiles, concavity–flat surface correspondence was repeated in the B–B′ profiles, where the linear steps perpendicular to B–B′ corresponded to the CP-1 plane for the R crystal and the CP-3 plane for the L crystal (indicated by arrows in Fig. 8(f)). On the other hand, the correspondence of the line profiles of C–C′ showed a peak-and-valley type (Fig. 8(g)), while the liner steps perpendicular to C–C′ were composed of the CP-2 planes for each crystal.

To clarify the relationship between the fracture surface geometry and martensitic transformation in more detail, t-EBSD analysis was applied to the substructure below the fracture surface, as shown **Fig. 9**. A pair of thin foil samples were milled along the lines of B–B′ in Figs. 8(a) and 8(b) from both halves of the fracture surfaces. Figure 9(a) shows a pair of cross-sectional SEM micrographs after FIB milling of both fracture surfaces. The red and black lines in Fig. 9(a) illustrate the brink of the fracture surface, which are in good agreement with the profile data of B–B′ in Fig.

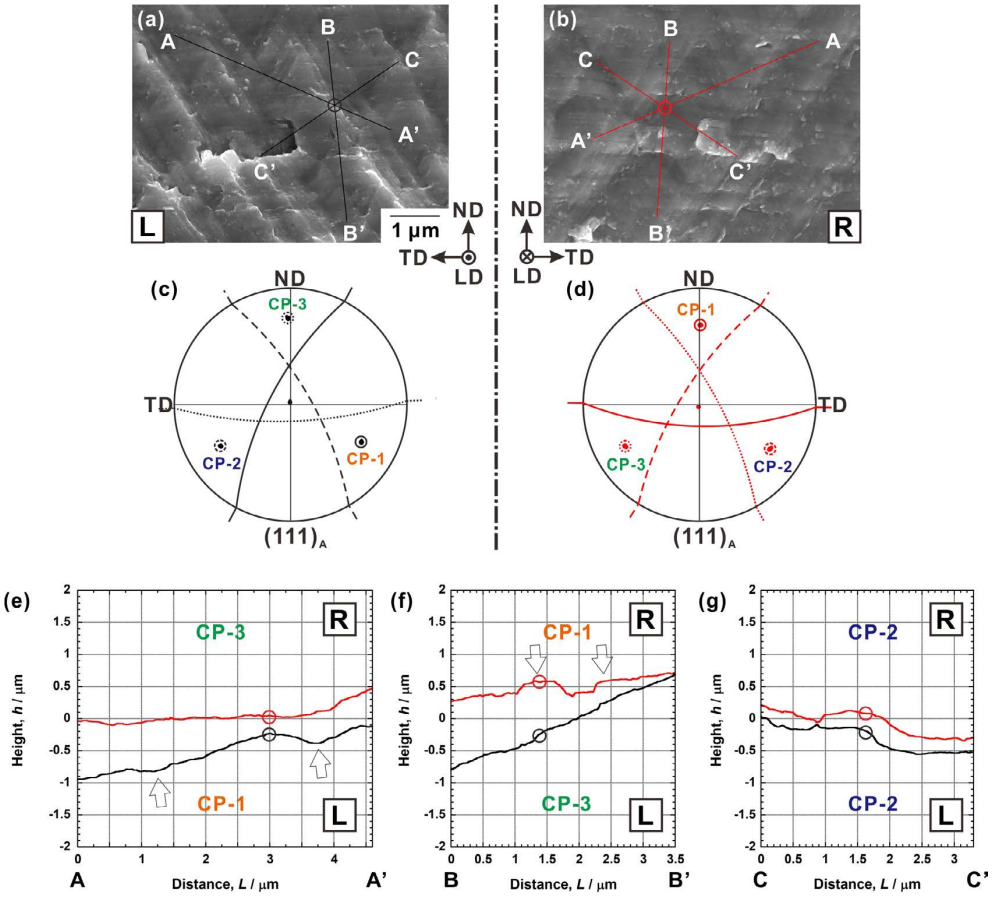

Fig. 8. (a) SEM micrograph indicative of the fracture surface of the boxed region in Fig. 7(d), and (b) the counterpart of (a), (c and d) $(111)_A$ pole figures of parent austenite in each crystal, which corresponding to (a and b), respectively (solid-, broken- and dotted-lines correspond to the CP-1, CP-2, and CP-3 planes, respectively). The matching of the line profiles for (e) A–A′, (f) B–B′ and (g) C–C′ in each fracture surface of (a and b), where circled positions in (e, f and g) correspond to the triple point of lines in (a and b). (Online version in color.)

8(f). The insets in Fig. 9(a) show the EBSD colour-coded maps for the boxed region, which distinguish austenite and martensite variants. The corresponding $(011)_M$ pole figures of martensite are shown in Figs. 9(b) and 9(c), which are overlaid with the $(111)_A$ pole figures of the parent austenite crystals. In both L and R crystals, a lamellar microstructure composed of martensite and retained austenite was observed in the substructure below the fracture surface. For each crystal, the martensite region was distributed along the deformation bands, where the CP-1 martensite variants dominated. Furthermore, the concavities in the R crystal were located at the region, where the CP-1 martensite was distributed in the substructure below the fracture surface (indicated by the arrows in Fig. 9(a)). When the CP-1 martensite variants are formed in each crystal, the excess hydrogen can diffuse out of the dynamically formed martensite towards the neighbouring pre-existing austenite across the twin boundary, based on the same mechanism as in the SC-H specimen. In our previous study,[19] it was reported that the hydrogen-induced twin boundary separation occurred predominantly at the interface between martensite and austenite. In addition, based on magnetic force microscopy observations of hydrogen-induced cracks,[28] it has been argued that α' martensite not only provides a path for rapid hydrogen diffusion, but also promotes crack initiation at the boundary between martensite-rich and austenite-rich regions. Therefore, this justifies the excess hydrogen concentrates at the twin boundary. Meanwhile, the local hydrogen concentration in the retained austenite at the twin boundary may induce dislocations and localised slip. Although the type of twin differs from annealing twin in the present study, thermal desorption analyses on a Fe-18Mn-1.5Al-0.6C austenitic steel,[29] to which a large amount of mechanical twins had been introduced by deformation, has revealed that the estimated activation energies for desorption of hydrogen from dislocations and twin boundaries were ~35 kJ/mol and ~62 kJ/mol, respectively. This means that de-trapping of hydrogen is more likely to occur in dislocations than in twin boundaries. Ulmer and Altstetter[30] have reported that under high hydrogen concentrations, inter-granular cracking occurs, even in the case of a type 310S stable austenitic steel, which is resistant to HE. These arguments suggest that local hydrogen concentration due to martensitic transformation weakens the interatomic bonding of the twin boundary, leading to cracking at the twin boundary before the quasi-cleavage along the habit planes of the CP-1 martensite.

Assuming that the cracking occurs as mentioned above, the cracks are locally formed at the twin boundary concurrently with the formation of the CP-1 martensite, as schematically shown in **Fig. 10**(a). Here, it should be noted that the correspondence of the line profiles of C–C′ reveals a peak-and-valley type (Fig. 8(g)), which corresponds to the intersection of the twin plane with the CP-2 planes in both crystals. In addition, the CP-2 martensite variant was formed in both crystals in the retained austenite of the substructure below the fracture surfaces. In the R crystal a small fraction of the CP-3 martensite was also formed (Fig. 9). The excess-hydrogen-assisted slip localisation in the retained austenite may produce high stress concentration at the crack tip formed along the twin boundary, leading to rapid coalescence of cracks. Therefore, martensite variants of CP-2 and CP-3 may be complementarily formed in conjunction with the final fracture. In our previous study of hydrogen-induced twin boundary separation in type 304 steel under cyclic load-

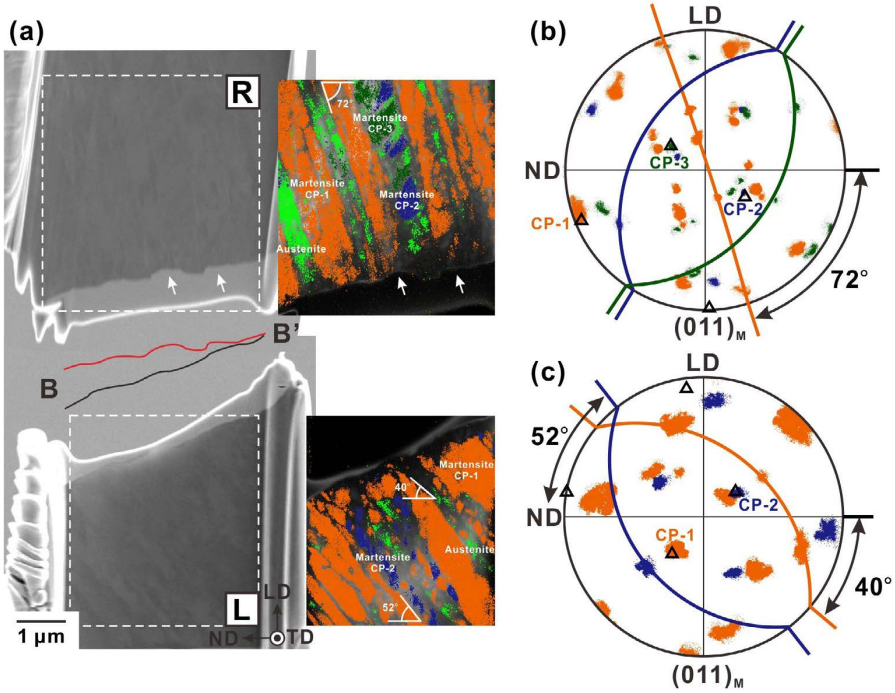

Fig. 9. (a) Matching of the SEM micrographs in the longitudinal cross-section parallel to the line of B–B' in Fig. 7. The insets in (a) show the EBSD colour-coded maps—which distinguish austenite and martensite variants—taken in the areas marked by the boxes in the L- and R-crystals. (b and c) $(011)_M$ pole figures of martensite corresponding to the colour-coded maps of the R- and L- crystals in (a), respectively (orange, blue, and green marks represent CP-1, CP-2, and CP-3, respectively). $(111)_A$ poles of parent austenite crystal are also shown as triangles, and they are labelled CP-1 to CP-3, respectively. (Online version in color.)

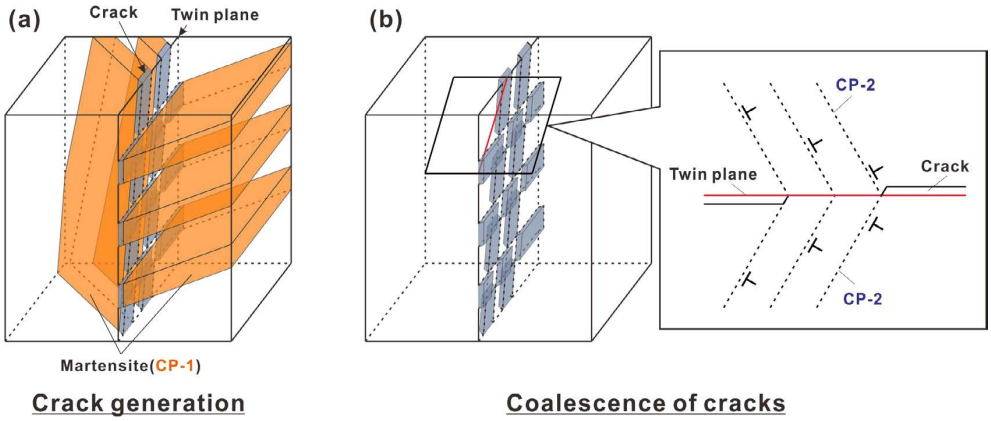

Fig. 10. Schematic illustration showing (a) the generation of cracks at the twin boundary due to the deformation-induced martensitic transformation, and (b) the coalescence of cracks through alternating shear on the CP-2 slip planes situated symmetrically with respect to the twin plane. (Online version in color.)

ing,[19] it was reported that hydrogen facilitates crack growth by alternating slips in the high applied stress conditions at the crack tip. These arguments suggest that the coalescence of cracks occurred through the hydrogen-enhanced alternating shear on the slip planes situated symmetrically with respect to the twin plane, as shown in Fig. 10(b).

4. Conclusions

Micro-tensile tests were performed on single crystals and twinned bi-crystals with and without hydrogen pre-charging in a type 304 metastable austenitic steel to mechanistically understand hydrogen-induced twin boundary separation. The conclusions are summarised as follows:

(1) In the stress–strain behaviour of single crystalline specimens, the hydrogen-charged specimen exhibited two-step work hardening behaviour, whereas the uncharged specimen showed nearly linear hardening behaviour. The hydrogen-charged twinned bi-crystalline specimen exhibited premature failure before the transition to the second stage of work hardening. Under hydrogen pre-charging conditions, the presence of a twin boundary perpendicular to the loading direction changed the fracture mode from the quasi-cleavage to premature failure with the twin boundary separation.

(2) Linear steps in three directions, which correspond to the intersections between the twin plane and the other {111} planes in austenite, were observed on the flat-facetted fracture surface caused by the hydrogen-induced twin boundary separation. Matching halves of the fracture surface along the three directions perpendicular to the linear steps revealed two sets of concavity–flat surface and a peak-and-valley correspondence. In the substructure below the fracture surface, martensite variants developed mainly with their habit planes parallel to the most favourably shear-stressed plane in each crystal, and they grew towards the concavities on the fracture surfaces.

(3) Based on the 3D-SEM analysis of the fracture surface, combined with t-EBSD analysis on deformation microstructures, we can propose the mechanism for hydrogen-induced twin boundary separation that was triggered by the cracking caused by high hydrogen concentration at the twin boundary associated with deformation-induced martensitic transformation, and that was followed by the coalescence of cracks through hydrogen-enhanced alternating shear on the slip planes situated symmetrically with respect to the twin boundary.

Acknowledgements

This work was supported in part by an ISIJ Research Promotion Grant and in part by the Iketani Science and Technology Foundation (ISTF).

REFERENCES

1) L. Zhang, M. Wen, M. Imade, S. Fukuyama and K. Yokogawa: *Acta Mater.*, **56** (2008), 3414.
2) T. Kanezaki, C. Narazaki, Y. Mine, S. Matsuoka and Y. Murakami: *Int. J. Hydrog. Energy*, **33** (2008), 2604.
3) C. San Marchi, T. Michler, K. A. Nibur and B. P. Somerday: *Int. J. Hydrog. Energy*, **35** (2010), 9736.
4) Y. Mine and T. Kimoto: *Corros. Sci.*, **53** (2011), 2619.
5) C. L. Briant: *Metall. Trans. A*, **10** (1979), 181.
6) G. R. Caskey, Jr.: Hydrogen Compatibility Handbook for Stainless Steel, E. I. du Pont de Nemours & Co., Savannah River Laboratory, Aiken, SC, (1983), DP-1643.
7) G. Han, J. He, S. Fukuyama and K. Yokogawa: *Acta Mater.*, **46** (1998), 4559.
8) D. Sun, G. Han, S. Vaodee, S. Fukuyama and K. Yokogawa: *Mater. Sci. Technol.*, **17** (2001), 302.
9) R. B. Benson, Jr., R. K. Dann and L. W. Roberts, Jr.: *Trans. Metall. Soc. AIME*, **242** (1968), 2199.
10) H. Hanninen and T. Hakarainen: *Metall. Trans. A*, **10** (1979), 1196.
11) L. W. Tsay, M. C. Young and C. Chen: *Corros. Sci.*, **45** (2003), 1985.
12) D. Eliezer, D. G. Chakrapani, C. J. Altstetter and E. N. Pugh: *Metall. Trans. A*, **10** (1979), 935.
13) R. Liu, N. Narita, C. Altstetter, H. Birnbaum and E. N. Pugh: *Metall. Trans. A*, **11** (1980), 1563.
14) G. Schuster and C. Altstetter: *Metall. Trans. A*, **14** (1983), 2085.
15) Y. Mine, C. Narazaki, K. Murakami, S. Matsuoka and Y. Murakami: *Int. J. Hydrog. Energy*, **34** (2009), 1097.
16) Y. Mine, K. Koga, O. Kraft and K. Takashima: *Scr. Mater.*, **113** (2016), 176.
17) G. R. Caskey, Jr.: *Scr. Meall.*, **11** (1977), 1077.
18) H. Jackson, C. San Marchi, D. Balch, B. Somerday and J. Michael: *Metall. Mater. Trans. A*, **47** (2016), 4334.
19) S. Ueki, Y. Mine and K. Takashima: *Corros. Sci.*, **129** (2017), 205.
20) Y. Higo, F. Lecroisey and T. Mori: *Acta Metall.*, **22** (1974), 313.
21) M. Kato and T. Mori: *Acta Metall.*, **24** (1976), 853.
22) T. Ito, Y. Mine, M. Otsu and K. Takashima: *J. Jpn. Inst. Met. Mater.*, **80** (2016), 22 (in Japanese).
23) Y. Mine, K. Hirashita, M. Matsuda, M. Otsu and K. Takashima: *Corros. Sci.*, **53** (2011), 529.
24) T. Tsurui, S. Inoue, K. Matsuda, H. Ishigaki, K. Murata and K. Koterazawa: *J. Soc. Mater. Sci. Jpn.*, **50** (2001), 1115 (in Japanese).
25) A. E. Pontini and J. D. Hermida: *Scr. Mater.*, **37** (1997), 1831.
26) Y. Mine and Z. Horita: *Mater. Trans.*, **53** (2012), 773.
27) Y. Mine, Z. Horita and Y. Murakami: *Acta Mater.*, **57** (2009), 2993.
28) L. Zhang, B. An, S. Fukuyama, T. Iijima and K. Yokogawa: *J. Appl. Phys.*, **108** (2010), 063526.
29) K. H. So, J. S. Kim, Y. S. Chun, K. T. Park, Y. K. Lee and C. S. Lee: *ISIJ Int.*, **49** (2009), 1952.
30) D. G. Ulmer and C. J. Altstetter: *Acta Metall. Mater.*, **39** (1991), 1237.